agreement with the known physiological adaptation to temperature of the tetraether membrane lipid composition in cultured hyperthermophilic Archaea and their marine mesophilic descendants[29]. Previous studies have also shown that the TEX_{86} parameter is not sensitive to salinity or depositional redox conditions[29,30]. Furthermore, initial applications show that reconstructed SSTs for Cretaceous sediments agree well with those derived from oxygen-isotope ratios of pristine skeletal carbonate[16].

Bulk organic isotopes and TOC contents were determined by decalcifying powdered rock samples with 2 N hydrochloric acid and analysing the decalcified sediments in duplicate on a Carlo Erba 1112 Flash Elemental Analyser coupled to a Thermofinnigan Delta Plus isotope mass spectrometer. Analytical errors for TOC range from 0.3% to 2%, and for $\delta^{13}C_{org}$ (‰ versus VPDB) are <0.1‰.

Received 10 June; accepted 28 October 2004; doi:10.1038/nature03143.

1. Clark, D. L. Early history of the Arctic Ocean. *Paleoceanography* **3,** 539–550 (1988).
2. Clark, D. L., Byers, C. W. & Pratt, L. M. Cretaceous black mud from the central Arctic Ocean. *Paleoceanography* **1,** 265–271 (1986).
3. Mudie, P. J. & Blasko, S. M. in *Initial Geological Report on CESAR: The Canadian Expedition to Study the Alpha Ridge* (eds Jackson, H. R., Mudie, P. J. & Blasko, S. M.) 59–99 (Paper 84–22, Geol. Surv. Canada, Ottawa, 1985).
4. Firth, J. V. & Clark, D. L. An early Maastrichtian organic-walled phytoplankton cyst assemblage from an organic-walled black mud in Core Fl-533, Alpha Ridge: evidence for upwelling conditions in the Cretaceous Arctic Ocean. *Mar. Micropaleont.* **34,** 1–27 (1998).
5. Jokat, W. Seismic investigations along the western sector of Alpha Ridge, Central Arctic Ocean. *Geophys. J. Int.* **152,** 185–201 (2003).
6. Schouten, S., Hopmans, E. C., Schefuß, E. & Sinninghe Damsté, J. S. Distributional variations in marine crenarchaeotal membrane lipids: a new tool for reconstructing ancient sea water temperatures? *Earth Planet. Sci. Lett.* **204,** 265–274 (2002).
7. Gradstein, F. M. *et al.* A Mesozoic time scale. *J. Geophys. Res. B* **99,** 24051–24074 (1994).
8. Dell'Agnese, D. J. & Clark, D. L. Siliceous microfossils from the warm Late Cretaceous and Early Cenozoic Arctic Ocean. *J. Paleontol.* **68,** 31–47 (1994).
9. Stoffyn-Egli, P. Iron and manganese micro-precipitates with a Cretaceous biosiliceous ooze from the Arctic Ocean: possible hydrothermal source. *Geo-Mar. Lett.* **7,** 223–231 (1987).
10. Mudie, P. J. in *Initial Geological Report on CESAR: The Canadian Expedition to Study the Alpha Ridge* (eds Jackson, H. R., Mudie, P. J. & Blasko, S. M.) 148–174 (Paper 84–22, Geol. Surv. Canada, Ottawa, 1985).
11. Barron, J. A. in *Initial Geological Report on CESAR: The Canadian Expedition to Study the Alpha Ridge* (eds Jackson, H. R., Mudie, P. J. & Blasko, S. M.) 137–148 (Paper 84–22, Geol. Surv. Canada, Ottawa, 1985).
12. Bukry, D. in *Initial Geological Report on CESAR: The Canadian Expedition to Study the Alpha Ridge* (eds Jackson, H. R., Mudie, P. J. & Blasko, S. M.) 125–135 (Paper 84–22, Geol. Surv. Canada, Ottawa, 1985).
13. Sinninghe Damsté, J. S. *et al.* The rise of the rhizosolenid diatoms. *Science* **304,** 584–587 (2004).
14. Holba, A. G. *et al.* Application of 24-norcholestanes for constraining source ages of petroleum. *Org. Geochem.* **29,** 1269–1283 (1998).
15. Kitchell, J. A. & Clark, D. L. Late Cretaceous–Paleogene paleogeography and paleocirculation: evidence of north polar upwelling. *Palaeogeogr. Palaeoclimatol. Palaeoecol.* **40,** 135–165 (1982).
16. Schouten, S. *et al.* Extremely high sea-surface temperatures at low latitudes during the middle Cretaceous as revealed by archaeal membrane lipids. *Geology* **31,** 1069–1072 (2003).
17. Barron, E. J. A warm, equable Cretaceous: the nature of the problem. *Earth Sci. Rev.* **19,** 305–338 (1983).
18. Barrera, E. & Savin, S. M. in *Evolution of the Cretaceous Ocean–Climate System* (eds Barrera, E. & Johnson, C. C.) 245–282 (Spec. Paper 332, Geol. Soc. Am., Boulder, Colorado, 1999).
19. Wilson, P. A. & Opdyke, B. N. Equatorial sea-surface temperatures for the Maastrichtian revealed through remarkable preservation of metastable carbonate. *Geology* **24,** 555–558 (1996).
20. Huber, B. T., Hodell, D. A. & Hamilton, C. P. Mid- to Late Cretaceous climate of the southern high latitudes. Stable isotopic evidence for minimal equator-to-pole thermal gradients. *Bull. Geol. Soc. Am.* **107,** 1164–1191 (1995).
21. Jenkyns, H. C., Gale, A. S. & Corfield, R. M. Carbon- and oxygen-isotope stratigraphy of the English Chalk and Italian Scaglia and its palaeoclimatic significance. *Geol. Mag.* **131,** 1–34 (1994).
22. Clarke, L. J. & Jenkyns, H. C. New oxygen-isotope evidence for long-term Cretaceous climate change in the Southern Hemisphere. *Geology* **27,** 699–702 (1999).
23. Morton, J. F. *Fruits of Warm Climates* (Creative Resources Systems, Miami, 1987).
24. Nathorst, A. G. Ueber die Reste eines Brotfruchtbaums ARTOCARPUS DICKSONI N. SP., aus den cenomanen Kreideablagerungen Grönlands. *Kongl. Svenska Vetenskaps-Akad. Hand* **24,** 2–9 (1890).
25. Tarduno, J. A. *et al.* Evidence for extreme climatic warmth from Late Cretaceous Arctic vertebrates. *Science* **282,** 2241–2244 (1998).
26. Huber, B. T. Tropical paradise at the Cretaceous poles? *Science* **282,** 2199–2200 (1998).
27. Herman, A. B. & Spicer, R. A. Palaeobotanical evidence for a warm Cretaceous Arctic Ocean. *Nature* **380,** 330–333 (1996).
28. Spicer, R. A. & Parrish, J. T. Late Cretaceous–early Tertiary palaeoclimates of northern high latitudes: a quantitative view. *J. Geol. Soc. Lond.* **147,** 329–341 (1990).
29. Wuchter, C., Schouten, S. & Sinninghe Damsté, J. S. Temperature-dependent variation in the distribution of tetraether membrane lipids of marine Crenarchaeota: Implications for TEX_{86} paleothermometry. *Paleoceanography* (in the press).
30. Schouten, S., Hopmans, E. & Sinninghe Damsté, J. S. The effect of maturity and depositional redox conditions on archaeal tetraether lipid palaeothermometry. *Org. Geochem.* **35,** 567–571 (2004).
31. Hay, W. W., Eicher, D. L. & Diner, R. in *Evolution of the Western Interior Basin* (eds Caldwell, W. G. E. & Kauffman, E. G.) 297–318 (Spec. Pap. 39, Geol. Ass. Canada, St John's, Newfoundland, 1993).

Acknowledgements We thank D. Clark for indicating the whereabouts of core Fl-533, and T. Simo for locating it in the Department of Geology and Geophysics of the University of Wisconsin at Madison. S. Rampen and J. Ossebaar (Royal NIOZ) are thanked for analytical assistance.

Competing interests statement The authors declare that they have no competing financial interests.

Correspondence and requests for materials should be addressed to H.C.J. (hughj@earth.ox.ac.uk).

Recycling lower continental crust in the North China craton

Shan Gao[1,2], Roberta L. Rudnick[3], Hong-Ling Yuan[1], Xiao-Ming Liu[1], Yong-Sheng Liu[2], Wen-Liang Xu[4], Wen-Li Ling[2], John Ayers[5], Xuan-Che Wang[2] & Qing-Hai Wang[4]

[1]*Key Laboratory of Continental Dynamics, Department of Geology, Northwest University, Xi'an 710069, China*
[2]*Faculty of Earth Sciences, China University of Geosciences, Wuhan 430074, China*
[3]*Geochemistry Laboratory, Department of Geology, University of Maryland, College Park, Maryland 20742, USA*
[4]*School of Earth Sciences, Jilin University, Changchun 130061, China*
[5]*Department of Geology, Vanderbilt University, PO Box 105 Station B, Nashville, Tennessee 37235, USA*

Foundering of mafic lower continental crust into underlying convecting mantle has been proposed as one means to explain the unusually evolved chemical composition of Earth's continental crust[1,2], yet direct evidence of this process has been scarce. Here we report that Late Jurassic high-magnesium andesites, dacites and adakites (siliceous lavas with high strontium and low heavy-rare-earth element and yttrium contents) from the North China craton have chemical and petrographic features consistent with their origin as partial melts of eclogite that subsequently interacted with mantle peridotite. Similar features observed in adakites and some Archaean sodium-rich granitoids of the tonalite-trondhjemite-granodiorite series have been interpreted to result from interaction of slab melts with the mantle wedge. Unlike their arc-related counterparts, however, the Chinese magmas carry inherited Archaean zircons and have neodymium and strontium isotopic compositions overlapping those of eclogite xenoliths derived from the lower crust of the North China craton. Such features cannot be produced by crustal assimilation of slab melts, given the high Mg#, nickel and chromium contents of the lavas. We infer that the Chinese lavas derive from ancient mafic lower crust that foundered into the convecting mantle and subsequently melted and interacted with peridotite. We suggest that lower crustal foundering occurred within the North China craton during the Late Jurassic, and thus provides constraints on the timing of lithosphere removal beneath the North China craton.

Eclogite forms by high- to ultrahigh-pressure metamorphism of basaltic rocks and has a density that is higher than that of peridotite by 0.2–0.4 g cm^{-3} (ref. 3). Because of this density contrast, mafic lower continental crust (together with the underlying lithospheric mantle) can be recycled into the mantle when granulite is transformed into eclogite during crustal thickening[1,4]. Such foundering may explain collapse of mountains, basin formation and associated magmatism, which is generated by asthenospheric upwelling into the space previously occupied by thickened lithosphere[5]. Density foundering may also explain the absence of high-pressure mafic residues that are the complement to the voluminous tonalite-

trondhjemite-granodiorite (TTG) gneisses found in Archaean cratons.

The eastern block of the North China craton (Fig. 1) is perhaps the best example of an Archaean craton that has lost its lithospheric keel[6–8] and is accordingly an ideal place to test the hypothesis of lower crustal foundering. Ancient remnants exposed at the surface or in lower crustal xenoliths[9,10] demonstrate the presence of early Archaean crust (≥3.6 Gyr old), whereas the more dominant late Archaean and Palaeoproterozoic U–Pb ages record significant later reworking[11] (see below). The contrasting compositions of mantle xenoliths carried in ~460 Myr diamondiferous kimberlites from those in nearby Neogene alkaline basalts record removal of the Archaean lithospheric mantle during the Phanerozoic[6–8], most probably during the Jurassic-Cretaceous[8,12], when the eastern block experienced significant reactivation, accompanied by extensive magmatism and large-scale basin formation. This voluminous magmatism, high surface heat flow[13], slow seismic wave speeds and thin crust and lithosphere[13,14] make the eastern block of the North China craton unique amongst Archaean cratons. This craton also has chemically evolved lower and bulk crust compositions[13]. The above lines of evidence have been used to infer that lower crustal recycling may have accompanied removal of the lithospheric mantle[13].

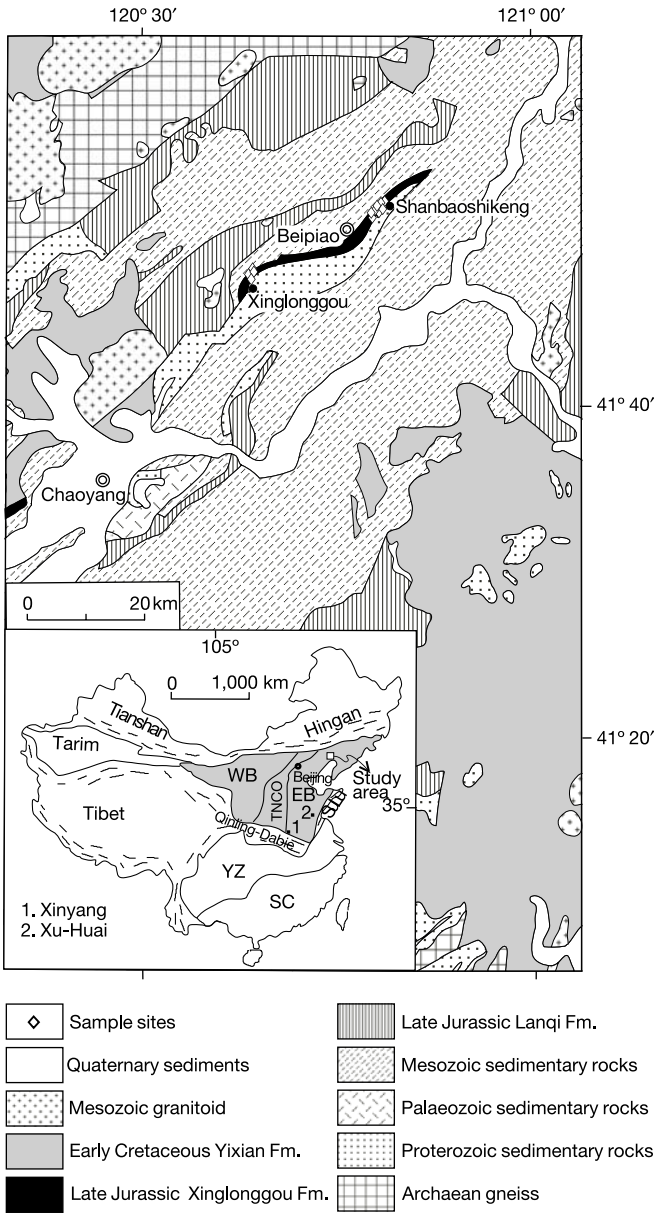

Figure 1 Geologic map of Western Liaoning Province, China. Our samples are from the Shanbaoshikeng and Xinglonggou type sections to the north and southwest of Beipiao, respectively. Inset shows major tectonic divisions of China, where YZ and SC denote the Yangtze craton and South China orogen, respectively. Also shown are the subdivisions of the North China craton[11], where WB, TNCO and EB denote the Western block, Trans-North China orogen and Eastern block, respectively. Numbers indicate the location of granulite, pyroxenite and eclogite xenoliths at (1) Xinyang and (2) Xu-Huai.

Mesozoic high-magnesium (Mg) volcanic rocks from Xinglonggou erupted along a narrow belt in the eastern block of the North China craton (western Liaoning Province, Fig. 1). The 403-m-thick Xinglonggou Formation consists of high-Mg andesites, adakites ($Na_2O/K_2O > 2.0$) and dacites (Mg# = 53–65, where Mg# = molar 100*Mg/(Mg + Fe)), interlayered with their lower Mg# (38–42) equivalents and rhyolites (Table 1). Euhedral, needle-shaped igneous zircons in two Xinglonggou rhyolites from the lower section yield concordant $^{206}Pb/^{238}U$ ages of 159 ± 3 Myr (2σ) (XL31) and 159 ± 4 Myr (XL34) (Fig. 2a; Supplementary Figs 1–3; Supplementary Table 1). Similar zircons from an aphanitic lava (XL03) from the upper section yields a less precise, younger age of 144 ± 9 Myr (Fig. 2a). Thus, the Xinglonggou lavas are Late Jurassic in age.

A striking feature of the Xinglonggou high-Mg adakites and dacites is the presence of octahedral chromite (Cr# = 65–81 in the core) and zoned orthopyroxene phenocrysts, which have a mantle with distinctively high Mg, Cr and Ni (Fig. 3; Supplementary Table 4). The sharp and irregular boundary between the core and mantle indicates that the latter formed as an overgrowth, with little diffusive exchange occurring between the two regions. This zoning reflects a significant increase in melt Mg# by reaction between the melt and a high-Mg environment (for example, mantle peridotite), whereas the very thin, low-Mg# rims probably represent magmatic orthopyroxene crystallized at crustal depths.

The presence of chromite and orthopyroxene are reflected in the unusually high whole-rock Cr (≤400 p.p.m.) and Ni (≤310 p.p.m.) contents. Other striking geochemical features of most Xinglonggou lavas include high Na_2O (≤5.7 wt%) and Sr (500–1,618 p.p.m.), and depletion in heavy rare-earth elements (HREEs; Yb < 1.8 p.p.m.) and Y (≤18 p.p.m.), with high Sr/Y (36–135) and La_N/Yb_N ratios (17–19; where subscript N denotes chondrite normalization) (Table 1). These features are characteristic of adakites from island arcs[15] and TTG that dominate areas of Archaean crust[16]. Like these rocks, the Xinglonggou lavas also show Nb–Ta depletion relative to La, and Pb enrichment relative to Ce (Supplementary Table 5).

Zircon age populations provide further evidence for the origin of these lavas. Although rhyolites contain primarily Mesozoic igneous zircons (Fig. 2a), inherited zircons dominate in adakites, andesites and dacites (for example, XL03 and XL18). The latter show a prominent age cluster at 2,500 Myr, which coincides with the major crustal growth period of the North China craton[11] (Fig. 2a–c). This inheritance pattern is consistent with zircon saturation systematics[17]. Magmatic orthopyroxene in the Xinglonggou andesites and dacites suggest that their temperature was >800 °C (ref. 18), but zircon saturation temperatures are lower (~760 °C, calculated for XL03 and XL18 having ~160 p.p.m. Zr)[17]. Thus, zircon is undersaturated in these melts and the observed crystals are xenocrysts, consistent with their old ages and sub-rounded morphologies (for example, XL18, Fig. 2b). Furthermore, if these melts formed from foundered lower crust, as we advocate below, they should be nearly anhydrous, which is consistent with the absence of hydrous phases in the Xinglonggou lavas. Harrison and Watson[19] calculate that it could take >100 Myr for a 50-μm-diameter zircon crystal to dissolve in an anhydrous granitic melt at 850 °C, which is consistent with the persistence of xenocrysts in these lavas. In contrast,

the rhyolites (XL31 and XL34) have significantly higher Zr (211–231 p.p.m.) and yield a zircon saturation temperature (820 °C) that is reasonable for these orthopyroxene-free magmas and consistent with the abundance of igneous zircons in the rhyolites.

Four origins have been proposed for adakites, high-Mg andesites and TTGs: (1) melting of subducted oceanic crust, followed by interaction with the overlying mantle wedge[15]; (2) melting of mantle peridotite under hydrous conditions[20]; (3) melting of thickened mafic lower continental crust[21], and (4) melting of foundered lower crust[5,22]. In all of these models except for (2), depletion in HREEs and Y requires melting of a mafic source rock within the stability field of garnet, most probably under eclogite-facies conditions.

The geochemical and mineralogical characteristics of the Xinglonggou lavas can be used to rule out a number of the above hypotheses. These lavas cannot have originated by melting in the lower continental crust, as chromite will not crystallize from such melts and the increase in Ni, Cr and Mg# in orthopyroxene requires interaction with peridotite after the melt formed. Likewise, the lavas cannot have formed by direct melting of peridotite or by crustal contamination of an original picritic melt, as these scenarios would predict high-Mg cores in the orthopyroxene, which is opposite to observation. Thus, the lavas may have originated as melts of either subducted oceanic crust or foundered lower crust with subsequent interaction of the melts with mantle peridotite. Indeed, the observed increase of Mg#, Ni and Cr of the melt (recorded in the orthopyroxene phenocrysts), together with orthopyroxene crystallization, are key features of slab melt-peridotite interaction[15,23].

The role played by Mesozoic subduction of the Palaeo-Pacific and Mongolo-Okhotsk oceanic plates in the genesis of the widespread volcanic and granitic magmatism along coastal eastern China (see, for example, ref. 24) is controversial. If a Mesozoic subduction zone did exist beneath eastern China, then the Xinglonggou lavas might have formed as slab melts. Adakites and associated high-Mg andesite from modern arcs that are interpreted as slab melts have mid-ocean-ridge basalt (MORB)-like Sr–Nd isotopic compositions, similar to those of the subducting oceanic crust (Fig. 4). In contrast, the Xinglonggou lavas have more evolved isotopic compositions (Fig. 4), with Nd model ages (T_{DM}) as old as 1.0 Gyr (Table 1). These isotopic signatures, together with the abundance of inherited Archaean zircons, requires that if the lavas originated by slab melting, they must have experienced significant crustal assimila-

Table 1 **Geochemical and Sr–Nd isotopic compositions of selected Xinglonggou lavas**

Sample	Lithology	Phenocrysts*	SiO_2	Al_2O_3	TFeO	MgO	CaO	Na_2O	K_2O	Mg#	Cr	Ni	Sr	Y	Zr	Yb	Sr/Y	La_N/Yb_N	Eu/Eu*
Geochemical compositions																			
XL01	HMDA		64.79	15.63	4.07	2.60	3.49	3.67	3.42	53	148	94	461	12	183	0.99	38	18	0.93
XL02	HMAD		63.11	15.12	3.98	3.54	5.15	3.56	1.24	61	137	85	716	9	163	0.98	80	17	0.98
XL03	HMAD	Opx†, Chm	63.09	15.25	4.02	3.56	5.28	3.35	1.30	61	149	89	765	11	162	1.1	70	17	0.84
XL04	HMAD	Opx†, Chm	62.59	15.27	4.08	3.64	5.47	3.28	1.16	61	147	86	836	13	162	1.1	64	17	0.84
XL05	HMAD	Opx†, Cpx, Chm	62.62	15.29	4.02	3.67	5.54	3.32	1.14	62	143	86	801	11	159	1.0	73	17	0.84
XL09	HMDA	Opx	64.86	15.26	3.77	2.93	3.54	3.78	3.37	58	127	82	491	13	161	1.1	38	18	0.84
XL12	HMAD	Chm	57.44	14.95	5.54	5.68	6.69	2.75	1.38	65	323	217	912	16	199	1.5	57	12	0.91
XL14	HMAN		57.35	15.71	7.02	4.47	5.46	3.34	2.37	53	313	246	626	19	201	1.9	33	10	0.90
XL15	AD	Ab	56.17	16.45	8.41	3.35	3.88	5.70	0.20	42	402	311	252	18	196	2.1	14	10	0.85
XL16	AN		59.15	16.51	6.88	2.33	2.51	5.36	3.38	38	344	310	613	17	210	1.8	36	11	0.96
XL17	DA		65.97	15.35	3.91	1.41	2.50	4.53	3.78	39	187	190	580	12	157	0.95	48	19	0.94
XL18	HMDA	Cpx	65.02	15.34	4.37	2.31	2.55	4.93	3.48	49	241	171	706	10	154	0.88	71	17	0.97
XL19	DA		66.00	15.48	3.99	1.63	1.99	5.14	3.75	42	231	166	729	10	162	0.88	73	18	0.98
XL20	HMDA	Cpx, Chm	62.94	15.00	5.23	2.60	2.70	3.87	3.55	47	337	105	617	15	154	1.4	41	11	0.94
XL21	HMDA		62.81	15.13	4.01	3.60	5.46	3.46	1.16	62	147	91	876	11	176	1.0	80	17	0.89
XL22	HMAD		62.22	15.46	4.15	3.81	5.59	3.16	1.25	62	137	92	1618	12	180	1.1	135	17	0.89
XL27	HMAD		62.05	15.22	4.11	3.72	5.40	3.39	1.23	62	130	90	763	12	174	1.1	64	17	0.87
XL31	RH		71.59	14.25	1.86	0.37	0.72	4.08	4.33	26	7.0	6.0	211	16	211	1.9	13	21	0.79
XL34	RH		70.92	14.96	2.08	0.35	0.83	5.26	3.52	23	22	41	231	21	231	2.0	11	19	0.71

Sample	$^{143}Nd/^{144}Nd$	2σ	$^{147}Sm/^{144}Nd$	$^{86}Sr/^{87}Sr$	2σ	$^{87}Rb/^{87}Sr$	T_{DM}
Isotopic compositions							
XL01	0.512489 ± 6		0.1091	0.707211 ± 4		0.7785	0.96
XL02	0.512471 ± 7		0.1065	0.706470 ± 4		0.1252	0.97
XL03	0.512511 ± 7		0.1074	0.705583 ± 15		0.1115	0.92
XL04	0.512448 ± 7		0.1074	0.705772 ± 20		0.0868	1.01
XL05	0.512511 ± 6		0.1076	0.705745 ± 16		0.0864	0.92
XL09							
XL12	0.512609 ± 7		0.1136	0.705338 ± 18		0.0671	0.82
XL14							
XL15	0.512667 ± 10		0.1203	0.705517 ± 17		0.0451	0.79
XL16	0.512668 ± 6		0.1197	0.706390 ± 16		0.3584	0.78
XL17	0.512575 ± 9		0.1101	0.706916 ± 16		0.5825	0.85
XL18	0.512556 ± 5		0.1126	0.706417 ± 14		0.4092	0.90
XL19	0.512525 ± 5		0.1116	0.706655 ± 13		0.4205	0.93
XL20	0.512567 ± 9		0.1183	0.707304 ± 11		0.4916	0.93
XL21	0.512413 ± 8		0.1074	0.705970 ± 13		0.0801	1.06
XL22	0.512442 ± 4		0.1071	0.706955 ± 11		0.0332	1.01
XL27	0.512517 ± 5		0.1070	0.706081 ± 12		0.1009	0.90
XL31							
XL34							

Major oxides are reported in weight per cent (wt%), trace elements in parts per million (p.p.m.) and T_{DM} in billion years (Gyr). TFeO, total iron as FeO; Mg#, molar 100*Mg/(Mg + Fe). $Eu/Eu^* = Eu_N/(Sm_N \times Gd_N)^{1/2}$, where subscript N denotes chondrite normalization. AD, adakite; AN, andesite; DA, dacite; HMAD, high-Mg adakite; HMAN, high-Mg andesite; HMDA, high-Mg dacite; RH, rhyolite. High-Mg rocks are defined as those with Mg# > 45. Ab, albite; Chm, chromite; Cpx, clinopyroxene; Opx, orthopyroxene. The Nd model age based on depleted mantle (T_{DM}) assumes a linear evolution of isotopic composition from ε Nd(T) = 0 at 4.56 Gyr to approximately +10 at the present time, and was calculated using the equation: $T_{DM} = (1/\lambda)\ \ln\{1 + [(^{143}Nd/^{144}Nd)_{sample} - 0.51315]/[(^{147}Sm/^{144}Nd)_{sample} - 0.2137]\}$, where the decay constant (λ) of ^{147}Sm used in the model age calculation is 0.00654 Gyr^{-1}.

*Determined by electron microprobe.

†Opx shows a contrasting lower-Mg core versus a higher-Mg mantle.

tion. However, there are no correlations between SiO_2 and initial Sr isotopic compositions at 130 or 160 Myr (correlation coefficient $r = 0.19$–0.32), which is inconsistent with the evolved isotopic compositions resulting from assimilation and fractional crystallization (AFC)-like processes in the lower crust (see Fig. 4 for models). Similarly, there is no correlation ($r = -0.11$ to 0.12) between initial $^{87}Sr/^{86}Sr$ and Rb contents in the Xinglonggou lavas, as would be expected if the high $^{87}Sr/^{86}Sr$ results from assimilation of high-Rb/Sr crust. The Xinglonggou high-Mg adakites, andesites and dacites do show positive correlations between initial $^{143}Nd/^{144}Nd$ and Cr and Ni ($r = 0.85$–0.89), which can be generated by interaction of the Xinglonggou adakitic melts with peridotite, whereby transition metal concentrations in the melt increase owing to consumption of olivine.

We propose that the Xinglonggou lavas formed by melting of foundered eclogite that formed at the base of Archaean lower crust that was thickened in the Triassic. The adakitic melts thus produced interacted with peridotite upon ascent to produce the high Mg, Cr and Ni signatures, the chromites and the zoned orthopyroxene phenocrysts.

Eclogite and garnet-clinopyroxenite xenoliths in Mesozoic volcanoclastic diatremes at Xinyang[25] and Mesozoic dioritic-monzodioritic porphyries at Xu-Huai[26] (Fig. 1) document the existence of eclogite within the deep (1.3–1.7 GPa) lithosphere of the North China craton during the Mesozoic. The Xu-Huai eclogite yields a whole rock-garnet Sm–Nd isochron of 219 ± 5 Myr (ref. 26), which overlaps with the 220–240 Myr eclogite-facies metamorphism in the Dabie-Sulu ultrahigh-pressure metamorphic belt (ref. 27 and references therein). U–Pb dates of the few available zircons from the Xu-Huai xenoliths reveal inheritance ages of 2.3–2.5 and 1.7–2.0 Gyr (Supplementary Table 6). Thus the eclogites formed in the Triassic from pre-existing Archaean lower crust, are not related to Jurassic-Cretaceous subduction of Palaeo-Pacific and Mongolo-Okhotsk oceanic crusts, and could be a plausible source for the adakitic melts. Indeed, modelling of the Sr–Nd isotopic compositions (Fig. 4) and Ni–Cr concentrations (not shown) of the

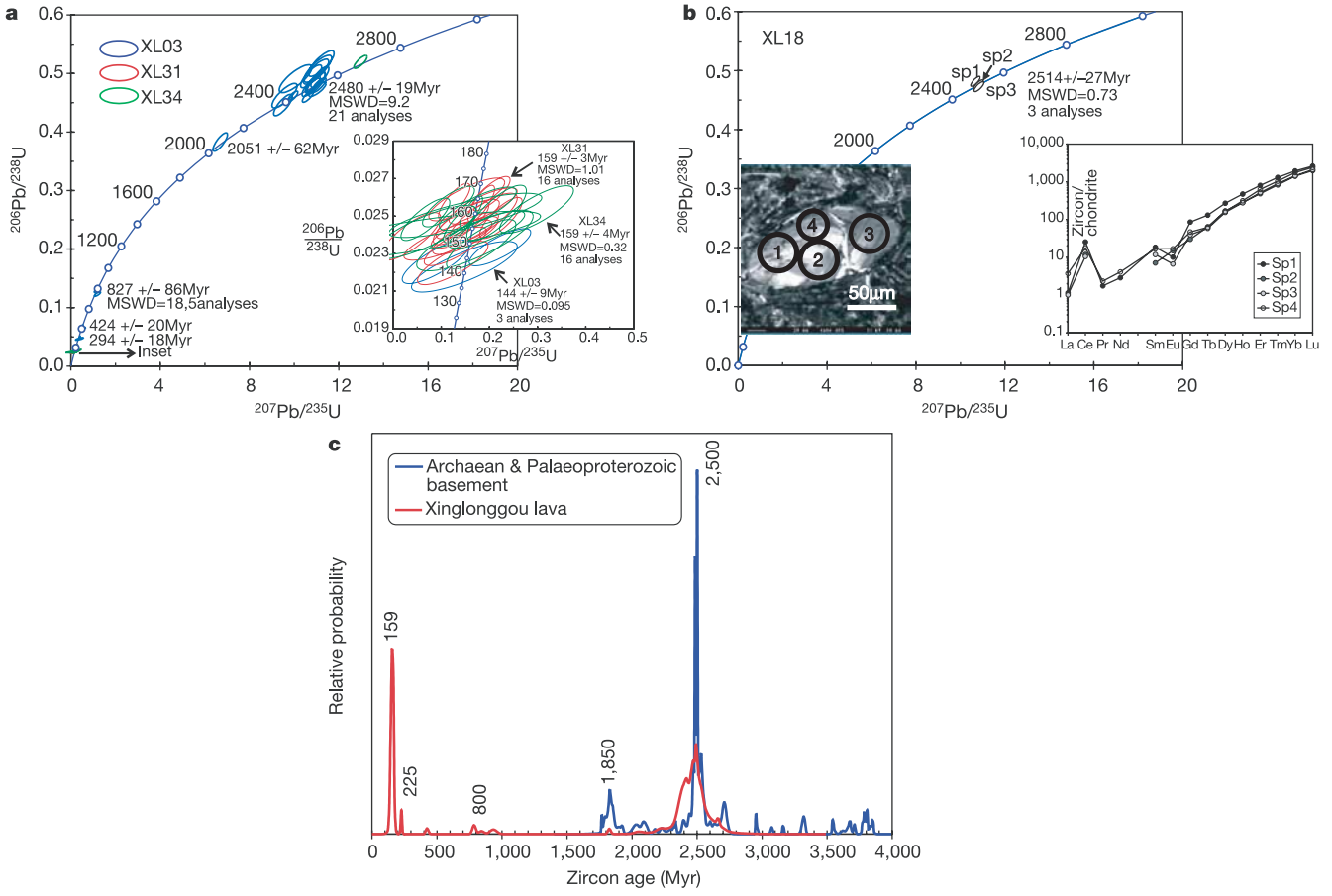

Figure 2 Zircon ages of the Xinglonggou lavas compared to those of the North China Archaean and Palaeoproterozoic basement. Concordia plots for zircons from **a**, high-Mg adakite (XL03) and rhyolites (XL31 and XL 34), and **b**, high-Mg dacite (XL18). Data for XL03, XL31 and XL34 were determined by SHRIMP II. Inset in **a** shows concordia plot for euhedral, needle-shaped zircons of volcanic origin in the rhyolites (Supplementary Figs 1–3; Supplementary Table 1). Igneous zircons from the overlying lava, XL03, are significantly finer-grained (<50 μm in diameter), consistent with its aphantic texture, and yield a slightly younger weighted mean $^{206}Pb/^{238}U$ age of 144 ± 9 Myr. Three 40-μm spots (Sp1, 2 and 3) of a large (75 × 163 μm), sub-rounded, inherited zircon from XL18 were measured in thin section for both the U–Pb age and REE concentrations by excimer LA-ICP-MS (Supplementary Tables 2, 3). An additional 30-μm spot (Sp4) was analysed only for REE composition. Left inset in **b** shows cathodoluminescence image of this zircon with spot locations marked. Right inset shows chondrite-normalized REE distributions of the four spots. Error ellipses are shown at 1σ. Ages with MSWD are the weighted mean $^{207}Pb/^{206}Pb$ age of zircons older than 1,000 Myr and weighted mean $^{206}Pb/^{238}U$ ages for zircons younger than 1,000 Myr. Uncertainties in ages are quoted at the 95% confidence level (2σ). Note that the Archaean ages for XL03 and XL18 are within error of each other. **c**, Comparison of zircon age distribution between Xinglonggou lavas (red) and North China Archaean and Palaeoproterozoic basement (blue). Ages for the Archaean and Palaeoproterozoic basement are from the literature, and were determined by SHRIMP and the single grain evaporation $^{207}Pb/^{206}Pb$ method (see Supplementary Data). The $^{207}Pb/^{206}Pb$ age is used for zircons older than 1,000 Myr, while the $^{206}Pb/^{238}U$ age is used for younger ones.

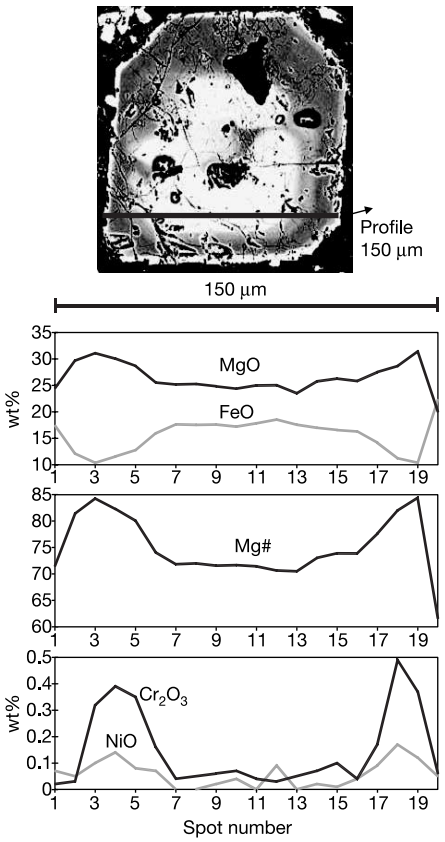

Figure 3 Compositional variations in an euhedral orthopyroxene phenocryst along the [001] crystallographic plane from Xinglonggou high-Mg adakite XL03. In the backscattered electron image (top) the dark areas are Mg-rich and the light areas are Fe-rich. In contrast to the grain's core, its mantle shows higher MgO, Cr and Ni contents, which reduce sharply in the very thin rim. The sharp and irregular boundary between the grain's core and mantle indicates that the mantle is a later overgrowth by chemical reaction, with little diffusive exchange between the two regions. In contrast, the mantle–rim boundary is regular.

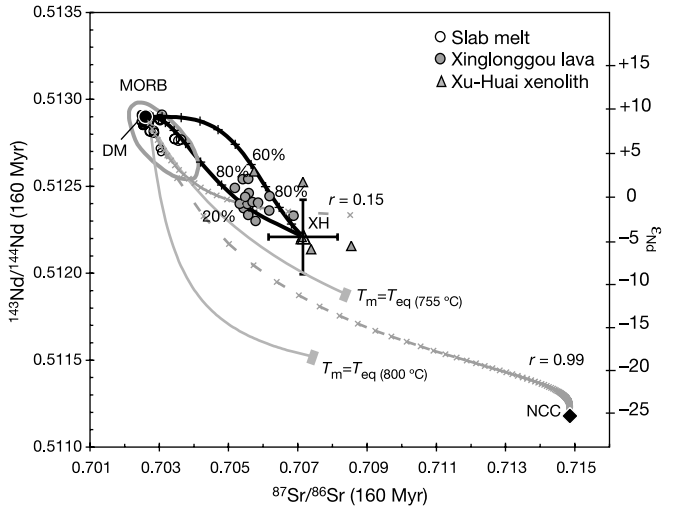

Figure 4 Sr–Nd isotopic compositions of the Xinglonggou lavas (this work, calculated at 160 Myr, the time of volcanic eruption) and inferred modern slab melts (open circles; small open circles indicate associated basalts). The thick black curves with pluses are AFC (assimilation and fractional crystallization) trends showing 10% increments in F (magma remaining) for a 30% partial melt of the median Xu-Huai eclogite-garnet clinopyroxenite (XH; large open triangle with 1σ error bars) that assimilates mantle (DM) with the isotopic composition of mid-ocean ridge basalt (MORB). The two trends represent melts derived from xenoliths with the highest (upper curve) and lowest (lower curve) Sr–Nd contents, respectively. Also shown are AFC and energy-constrained AFC (EC-AFC) models for assimilation of slab melt by the North China crust (NCC). The AFC trend (grey broken thin curve with crosses indicating 5% increment in F) passes through the Xinglonggou data only for a very low rate of assimilation ($r \leq 0.15$), with less than 20% melt left after assimilation. Using the highest Cr (636 p.p.m.) and Ni (132 p.p.m.) contents in Aleutian high-Mg andesites/adakites as representative of adakite before continental crust assimilation, the modelled Cr and Ni in the corresponding melt is <2 p.p.m., which is far lower than observed in the Xinglonggou adakites and andesites (Table 1). EC-AFC trends (grey thin curves) for equilibration temperatures (T_{eq}) of 800 °C and 755 °C are shown. The EC-AFC trend passes through the Xinglonggou data only when the equilibration temperature is very close to assimilant solidus temperature (that is, <4 °C difference) (not shown for clarity). Such temperatures are considerably lower than the temperature (>800 °C) suggested by the presence of orthopyroxene phenocrysts and zircon saturation thermometry (as discussed in the main text). The above modelling indicates that the Xinglonggou lavas probably formed by consumption of <40% melt during reaction with the mantle, and did not originate from crustal assimilation of a slab melt. See Supplementary Discussion for a detailed explanation, data sources and modelling parameters.

Xinglonggou lavas suggests their derivation from a source region similar to the Xu-Huai eclogites and garnet clinopyroxenites, with subsequent assimilation (at <40% magma consumption) of peridotite having an isotopic composition of MORB.

As dynamical models show[4], density foundering of lower crust is likely to be accompanied by removal of lithospheric mantle. The latter was previously documented in the eastern block of the North China craton[6–8], and probably occurred during the Late Jurassic or Early Cretaceous[8,12]. Our data indicate that foundering was initiated by 159 Myr ago and probably was protracted (lasting into the Early Cretaceous). However, the mechanism triggering the density instability and foundering is still an open question. It may have been related to subduction of the Palaeo-Pacific Ocean, to collision of an amalgamated North China-Mongolian plate with the Siberian plate during closure of a Mongolo-Okhotsk ocean[24], or to more global events, like mantle overturn[12]; it is also possible that a combination of all three of these mechanisms triggered the density instability, as they may all have operated during the Jurassic-Cretaceous. Upwelling of hot asthenosphere at the base of the crust followed lithospheric removal, and caused the intense tectonic reactivation and crustal melting that characterizes the North China craton, with production of highly fractionated granites (which host the most important Au–Cu and rare metal mineralization in eastern China) between 120 and 130 Myr ago[28]. This was followed by basin formation and eruption of asthenosphere-derived alkali basalts that started 100 Myr ago and lasted to the Holocene[7]. All these events are consequences of lower crustal and lithospheric mantle foundering[1,2,4,5]. □

Methods

U–Pb dating

Zircons from the volcanic rocks were dated on a SHRIMP II at the Beijing SHRIMP Center and on an excimer (193 nm wavelength) laser ablation inductively coupled plasma mass spectrometer (LA-ICP-MS) at the Key Laboratory of Continental Dynamics, Northwest University. The ICP-MS used is an Elan 6100 DRC (Dynamic Reaction Cell) from Perkin Elmer/SCIEX (Canada). The GeoLas 200M laser-ablation system (MicroLas, Göttingen, Germany) was used for the laser ablation experiments. Backscatter electron and cathodoluminescence images (Supplementary Figs 1–3) were made of the zircons before analyses. Uncertainties in ages are quoted at the 95% confidence level (2σ). Spot diameter was 30 and 30–40 μm for SHRIMP II and LA-ICP-MS, respectively. Common Pb corrections were made using measured ^{204}Pb (Supplementary Tables 1, 6).

The SHRIMP II analyses followed established methods[29]. The calibration standard is Sri Lankan gem zircon standard (SL13), and the internal standard is the Australian National University zircon standard TEMORA 1 (ref. 30).

For LA-ICP-MS analysis, raw count rates were measured for ^{29}Si, ^{204}Pb, ^{206}Pb, ^{207}Pb, ^{208}Pb, ^{232}Th and ^{238}U. U, Th and Pb concentrations were calibrated by using ^{29}Si as an internal standard and NIST SRM 610 as the reference standard. ^{202}Hg is usually <10 counts per second in the gas blank. Therefore, the contribution of ^{204}Hg to ^{204}Pb was negligible and no correction was made. $^{207}Pb/^{206}Pb$, $^{206}Pb/^{238}U$ and $^{208}Pb/^{232}Th$ ratios

were calculated using GLITTER 4.0 (Macquarie University), which were then corrected for both instrumental mass bias and depth-dependent elemental and isotopic fractionation using Harvard zircon 91500 as external standard. The ages were calculated using ISOPLOT[31]. Our measurement of TEMORA 1 as an unknown yielded a weighted $^{206}Pb/^{238}U$ age of 415 ± 4 Myr (MSWD (mean squared weighted deviates) = 0.112, $n = 24$)[32], which is in good agreement with the recommended isotope dilution-thermal ionization mass spectrometry (ID-TIMS) age of 416.75 ± 0.24 Myr (ref. 30). Analytical details for age and trace and REE determinations of zircons are reported elsewhere[32].

Mineral analysis

Major element composition of minerals was analysed on a JEOL Superprobe JXA 8100 at the Department of Geology, Peking University, using an accelerating voltage of 15 kV, beam current 1×10^{-8} A and spot diameter of 1 μm.

Major and trace element analysis

Chemical compositions of whole rocks were measured at the Key Laboratory of Continental Dynamics, Northwest University. Major element compositions were analysed by X-ray fluorescence (XRF; Rikagu RIX 2100) using fused glass disks. Trace element composition was analysed by ICP-MS (Elan 6100 DRC) after acid digestion of samples in Teflon bombs. They were also analysed by XRF using powered rock pellets. Concentrations of Sr, Y, Nb, Zr, Cr and Ni obtained using these two methods for the same samples generally agree to within 10% uncertainty[33]. Analyses of United States Geological Survey rock standards (BCR-2, BHVO-1 and AGV-1) indicate precision and accuracy better than 5% for major elements and 10% for trace elements and REEs[33].

Sr–Nd isotopes

Sr–Nd isotopic compositions were determined on a Finnigan MAT-261 mass spectrometer operated in static mode at the Isotope Laboratory of China, University of Geosciences, Wuhan. Two aliquots of sample powder (200 mesh), ~100 mg each, were weighed with one aliquot being added to a mixed solution of ^{84}Sr, ^{85}Rb, ^{145}Nd and ^{149}Sm isotope spikes. Samples were digested in Teflon bombs with a mixture of concentrated HF, HNO_3 and $HClO_4$. Columns of AG50W-X8 and HDEHP resins were used sequentially for separation and purification of REEs and finally for separation of Nd and Sm by HCl eluants. The measured $^{143}Nd/^{144}Nd$ and $^{87}Sr/^{86}Sr$ ratios were normalized to $^{146}Nd/^{144}Nd = 0.721900$ and $^{88}Sr/^{86}Sr = 8.375209$, respectively. The La Jolla standard measured during the course of analyses gave an average $^{143}Nd/^{144}Nd$ of 0.511862 ± 5 (2σ, $n = 15$), and BCR-2 gives $^{143}Nd/^{144}Nd = 0.512635 \pm 4$, $^{147}Sm/^{144}Nd = 0.1369$, Nd = 29.10 p.p.m. and Sm = 6.591 p.p.m. NBS-987 gave $^{87}Sr/^{86}Sr = 0.710236 \pm 16$ (2σ, $n = 6$).

Received 27 May; accepted 3 November 2004; doi:10.1038/nature03162.

1. Kay, R. W. & Kay, S. M. Creation and destruction of lower continental crust. *Geol. Rundsch.* **80,** 259–278 (1991).
2. Rudnick, R. L. Making continental crust. *Nature* **378,** 571–578 (1995).
3. Rudnick, R. L. & Fountain, D. M. Nature and composition of the continental crust: a lower crustal perspective. *Rev. Geophys.* **33,** 267–309 (1995).
4. Jull, M. & Kelemen, P. B. On the conditions for lower crustal convective instability. *J. Geophys. Res.* **106,** 6423–6446 (2001).
5. Kay, R. W. & Kay, S. M. Delamination and delamination magmatism. *Tectonophysics* **219,** 177–189 (1993).
6. Menzies, A., Fan, W.-M. & Zhang, M. in *Magmatic Processes and Plate Tectonics* (eds Prichard, H. M., Alabaster, H. M., Harris, T. & Neary, C. R.) 71–81 (Geol. Soc., London, 1993).
7. Griffin, W. L., Zhang, A. D., O'Reilly, S. Y. & Ryan, C. G. in *Mantle Dynamics and Plate Interactions in East Asia* (eds Flower, M., Chung, S.-L., Lo, C.-H. & Lee, T.-Y.) 107–126 (American Geophysical Union, Washington DC, 1998).
8. Gao, S., Rudnick, R. L., Carlson, R. W., McDonough, W. F. & Liu, Y. S. Re-Os evidence for replacement of ancient mantle lithosphere beneath the North China Craton. *Earth Planet. Sci. Lett.* **198,** 307–322 (2002).
9. Liu, D.-Y., Nutman, A. P., Compston, W., Wu, J. S. & Shen, Q.-H. Remnants of > 3800 Ma crust in the Chinese part of the Sino-Korean craton. *Geology* **20,** 339–342 (1992).
10. Zheng, J. P. *et al.* 3.6 Ga lower crust in central China: New evidence on the assembly of the North China Craton. *Geology* **32,** 229–232 (2004).
11. Zhao, G. C., Wilde, S. A., Cawood, P. A. & Sun, M. Archean blocks and their boundaries in the North China Craton: lithological, geochemical, structural and P-T path constraints and tectonic evolution. *Precambr. Res.* **107,** 45–73 (2001).
12. Wilde, S. A., Zhou, X. H., Nemchin, A. A. & Sun, M. Mesozoic crust-mantle interaction beneath the North China craton: A consequence of the dispersal of Gondwanaland and accretion of Asia. *Geology* **31,** 817–820 (2003).
13. Gao, S. *et al.* How mafic is the lower continental crust? *Earth Planet. Sci. Lett.* **106,** 101–117 (1998).
14. Huang, Z. X., Su, W., Peng, Y. J., Zheng, Y. J. & Li, H. Y. Rayleigh wave tomography of China and adjacent regions. *J. Geophys. Res.* **108,** doi:10.1029/2001JB001696 (2003).
15. Kay, R. W. Aleutian magnesian andesites – melts from subducted Pacific ocean crust. *J. Volcanol. Geotherm. Res.* **4,** 117–132 (1978).
16. Martin, H. Adakitic magmas: modern analogues of Archaean granitoids. *Lithos* **46,** 411–429 (1999).
17. Watson, E. B. & Harrison, T. M. Zircon saturation revisited: Temperature and composition effects in a variety of crustal magma types. *Earth Planet. Sci. Lett.* **64,** 295–304 (1983).
18. Wolf, M. B. & Wyllie, P. J. Dehydration-melting of amphibolite at 10 kbar: the effects of temperature and time. *Contrib. Mineral. Petrol.* **115,** 369–383 (1994).
19. Harrison, T. M. & Watson, E. B. Kinetics of zircon dissolution and zirconium diffusion in granitic melts of variable water content. *Contrib. Mineral. Petrol.* **84,** 66–72 (1983).
20. Stern, R. A. & Hanson, G. N. Archean high-Mg granodiorite: a derivative of light rare earth element-enriched monzodiorite of mantle origin. *J. Petrol.* **32,** 201–238 (1991).
21. Atherton, M. P. & Petford, N. Generation of sodium-rich magmas from newly underplated basaltic crust. *Nature* **362,** 144–146 (1993).
22. Xu, J. F., Shinjo, R., Defant, M. J., Wang, Q. A. & Rapp, R. P. Origin of Mesozoic adakitic intrusive rocks in the Ningzhen area of east China: Partial melting of delaminated lower continental crust? *Geology* **30,** 1111–1114 (2002).
23. Rapp, R. P., Shimizu, N., Norman, M. D. & Applegate, G. S. Reaction between slab-derived melts and peridotite in the mantle wedge: experimental constraints at 3.8 GPa. *Chem. Geol.* **160,** 335–356 (1999).
24. Davis, G. A., *et al.* in *Paleozoic and Mesozoic Tectonic Evolution of Central Asia: From Continental Assembly to Intracontinental Deformation* (eds Hendrix, M. S. & Davis, G. A.) 171–197 (Memoir Geol. Soc. Am., Boulder, 2001).
25. Zheng, J. P., Sun, M., Lu, F. X. & Pearson, N. Mesozoic lower crustal xenoliths and their significance in lithospheric evolution beneath the Sino-Korean Craton. *Tectonophysics* **361,** 37–60 (2003).
26. Xu, W. L., Wang, D. Y., Liu, X. C., Wang, Q. H. & Lin, J. Q. Discovery of eclogite inclusions and its geological significance in early Jurassic intrusive complex in Xuzhou, northern Anhui, eastern China. *Chin. Sci. Bull.* **47,** 1212–1216 (2002).
27. Ayers, J. C., Dunkle, S., Gao, S. & Miller, C. F. Constraints on timing of peak and retrograde metamorphism in the Dabie Shan Ultrahigh-Pressure Metamorphic Belt, east-central China, using U–Th–Pb dating of zircon and monazite. *Chem. Geol.* **186,** 315–331 (2002).
28. Qiu, Y. M., Groves, D. I., McNaughton, N. J., Wang, L. G. & Zhou, T. H. Nature, age, and tectonic setting of granitoid-hosted, orogenic gold deposits of the Jiaodong Peninsula, eastern North China craton, China. *Mineralium Deposita* **37,** 283–305 (2002).
29. Williams, I. S. in *Applications of Microanalytical Techniques to Understanding Mineralizing Processes* (eds McKibben, M. A., Shanks, W. C. III & Ridley, W. I.) 1–35 (Reviews in Economic Geology, Vol. 7, Society of Economic Geologists, Littleton, Colorado, 1998).
30. Black, L. P. *et al.* TEMORA 1: a new zircon standard for Phanerozoic U–Pb geochronology. *Chem. Geol.* **200,** 155–170 (2003).
31. Ludwig, K. R. *ISOPLOT 3.00: A Geochronological Toolkit for Microsoft Excel* (Berkeley Geochronology Center, Berkeley, California, 2003).
32. Yuan, H. L. *et al.* Accurate U-Pb age and trace element determination of zircon by laser ablation-inductively coupled plasma mass spectrometry. *Geostand. Newsl.* (in the press).
33. Rudnick, R. L., Gao, S., Ling, W. L., Liu, Y. S. & McDonough, W. F. Petrology and geochemistry of spinel peridotite xenoliths from Hannuoba and Qixia, North China craton. *Lithos* **77,** 609–637 (2004).

Supplementary Information accompanies the paper on **www.nature.com/nature**.

Acknowledgements This research was supported by the National Natural Science Foundation of China, Chinese Ministry of Science and Technology and the Beijing SHRIMP Center (S.G. and H.L.Y.) and the NSF (R.L.R. and J.C.A). We thank D. Y. Liu, Z. C. Hu, G. M. Shu and Y. B. Wang for help in SHRIMP II and electron microprobe analyses, and D. Günther for help in setting up the LA-ICP-MS. This Letter benefited from comments and suggestions from S. Wilde and H. Rollinson.

Competing interests statement The authors declare that they have no competing financial interests.

Correspondence and requests for materials should be addressed to R.L.R. (rudnick@geol.umd.edu) or S.G. (sgao@263.net.cn).

The impact of surface-adsorbed phosphorus on phytoplankton Redfield stoichiometry

Sergio A. Sañudo-Wilhelmy[1], Antonio Tovar-Sanchez[1,2], Fei-Xue Fu[3], Douglas G. Capone[4], Edward J. Carpenter[5] & David A. Hutchins[3]

[1]*Marine Sciences Research Center, Stony Brook University, Stony Brook, New York 11794-5000, USA*
[2]*IMEDEA (CSIC-UIB), Instituto Mediterráneo de Estudios Avanzados, Esporles 07190, Mallorca, Islas Baleares, Spain*
[3]*College of Marine Studies, University of Delaware, 700 Pilottown Road, Lewes, Delaware 19958, USA*
[4]*Wrigley Institute of Environmental Studies and Department of Biological Sciences, University of Southern California, Los Angeles, California 90089, USA*
[5]*Romberg Tiburon Center, San Francisco State University, 3152 Paradise Drive, Tiburon, California 94920, USA*

The Redfield ratio of 106 carbon:16 nitrogen:1 phosphorus in marine phytoplankton[1] is one of the foundations of ocean biogeochemistry, with applications in algal physiology[2], palaeoclimatology[3] and global climate change[4]. However, this ratio varies substantially in response to changes in algal nutrient status[5] and taxonomic affiliation[6,7]. Here we report that Redfield ratios are also strongly affected by partitioning into surface-adsorbed